Journal of CO_2 Utilization 37 (2020) 20–28

Contents lists available at ScienceDirect

Journal of CO_2 Utilization

journal homepage: www.elsevier.com/locate/jcou

Experimental-theoretical study of the epoxide structures effect on the CO_2 conversion to cyclic carbonates catalyzed by hybrid titanate nanostructures

Wesley F. Monteiro[a], Michele O. Vieira[a], Eduardo F. Laschuk[b], Paolo R. Livotto[c], Sandra M.O. Einloft[a,b], Michèle O. de Souza[c], Rosane A. Ligabue[a,b,*]

[a] Graduate Program in Materials Engineering and Technology, Pontifical Catholic University of Rio Grande do Sul - PUCRS, Brazil
[b] School of Technology, Pontifical Catholic University of Rio Grande do Sul - PUCRS, Brazil
[c] Chemistry Institute, Federal University of Rio Grande do Sul - UFRGS, Brazil

ARTICLE INFO

Keywords:
CO_2 fixation
Titanate nanotubes
Ionic liquids
DFT
HOMO-LUMO gap

ABSTRACT

Hybrid nanostructures were produced from several ionic liquids (ILs) anchored on titanate nanotubes (TNT). Ionic liquids ILs composed by the 1-methyl-3-(3-trimethoxysilylpropyl)imidazolium cation associated with the $[Cl^-]$, $[BF_4^-]$, $[PF_6^-]$ or $[Tf_2N^-]$ anions were studied. The highest anchored amounts of IL were obtained with the $[Cl^-]$ and $[Tf_2N^-]$ anions, respectively, of 31.5 and 43.5 % w/w. These hybrid nanostructures were used in the direct conversion of CO_2 to cyclic carbonates through the coupling reaction with various epoxides (epichlorohydrin, styrene oxide, glycidyl isopropyl ether, and propylene oxide). With styrene oxide, the best results were obtained using the $[Cl^-]$ and $[BF_4^-]$ IL, showing TON values of 35.6 and 18.4, and TOF values of 17.2 and 9.2 h^{-1}, respectively. The TNT-[IL][Cl] was also used with different epoxides (*i.e.* epichlorohydrin, styrene oxide, glycidyl isopropyl ether and propylene oxide) being more reactive in the reactions with epichlorohydrin (TON = 86.3, TOF = 21.6 h^{-1}) and styrene oxide (TON = 47.0 TOF = 11.7 h^{-1}). Theoretical studies showed that the high reactivity of styrene oxide can be associated with their lower HOMO-LUMO energy gap, while epichlorohydrin presented high electron withdrawing effect by chlorine, generating the higher electronegativity. Besides that, by NBO analysis, both molecules presented lower donor – acceptor interact energy which may favor the opening of the ring.

1. Introduction

The world population is facing a major issue, the rise of global warming due to unrestricted emission of greenhouse gases. Among the greenhouse gas, CO_2 has the greatest adverse impact, causing approximately 55 % of the observed global warming [1]. One of the approaches to CO_2 mitigation is its capture [2,3] followed by its storage in geological sites [4]. Others options could be the use of CO_2 for beverage gasification, as a supercritical solvent, *etc.*, or using CO_2 as reactant leading to its chemical conversion [5] corresponding to a green approach [6,7].

As an example of CO_2 chemical conversion, the insertion of CO_2 in an epoxide molecule through cycloaddition that leads to cyclic carbonates production is one of the most successful and efficient routes for chemical fixation of CO_2 [8].

Cyclic carbonates can be used as green solvents, electrolytes for lithium-ion batteries and as intermediates in the production of polycarbonates, among others applications [9,10]. The development of efficient and selective catalysts for CO_2 cycloaddition reactions are the object of numerous studies in the last decades. Metal organic frameworks [11], azaphosphatranes compounds [12], dinuclear silver complexes [13] are new catalysts among others which are promissory compounds for the development these reaction in homogeneous medium.

Heterogeneous catalytical systems which are more environmentally friendly as they allow the recovery and reuse of the catalyst also are described in the literature. Baj et al. [14] developed a nanostructure-based on quaternary ammonium salt supported on carbon nanotubes. Sankar et al. [15] reported the synthesis and catalytic efficiency of imidazole anchored on SiO_2, and Liu et al. [16] synthesized a series of zwitterionic nanoparticles supported on mesoporous silica. Novelties about heterogeneous catalytic system active in CO_2 cycloaddition can surge based on new processes for the synthesis of supports with different morphology, as well as, hybrid nanostructures.

Use of methodology for the controlled deposition of TiO_2 overcoats, the development of multi-metal nanomaterials and nanostructured

* Corresponding author at: Graduate Program in Materials Engineering and Technology, Pontifical Catholic University of Rio Grande do Sul - PUCRS, Brazil.
E-mail address: rligabue@pucrs.br (R.A. Ligabue).

https://doi.org/10.1016/j.jcou.2019.11.024
Received 17 September 2019; Received in revised form 25 October 2019; Accepted 23 November 2019
Available online 30 November 2019
2212-9820/

ultrathin layer based on PtCo bimetallic nanotube applied for reaction of dehydration, reduction, and proton exchange, respectively, are some examples of impact of these research in the development of new materials and technologies [17–19]

Besides that, in recent years, studies regarding applications of ionic liquids (ILs) increased due to their useful properties such as low vapor pressure, high thermal and chemical stability, low combustibility, environment-friendly and unique solvating properties for many polar and non-polar compounds [20,21]. The use of ILs as functionalizing agents to get hybrid nanostructures has also received great attention. Imidazolium cation based-ionic liquid was immobilized on MOF's and used as a catalyst in the synthesis of propylene carbonate from CO_2 and propylene oxide under solvent-free conditions. The synergy between the nanostructure and the ionic liquid showed up important, leading to high yield (91 %) in propylene carbonate production compared to values obtained with the isolated structures (13 % with MOF and 9 % with IL) [22]. Appaturi and Adam reported interesting results corresponding to the production of phenyl glycidyl carbonate (96 % of conversion, 100 % of selectivity) under solvent-free conditions using as the catalyst imidazolium cation based-IL anchored on MCM-41 [23].

Recently, our group described as a pioneering study the synthesis of titanate nanotubes (TNTs) functionalized with silanized ionic liquid applied as the catalyst for the CO_2 conversion to propylene carbonate (PC) with high catalytic activity (TON = 276.8 and TOF = 46.1 h^{-1}) [24]. Based on these innovative structures, we report herein the synthesis of three new hybrid nanostructures employing TNTs, and ILs containing the same cation (the 1-methyl-3-(3-trimethoxysilylpropyl) imidazolium ([$(MeO)_3Sipmim^+$]) and different anions ([BF_4^-], [PF_6^-] and [Tf_2N^-]) applied in the CO_2 conversion to cyclic carbonates using different epoxides (propylene oxide (PO), glycidyl isopropyl ether (GIE), epichlorohydrin (ECH) and styrene oxide (SO).

2. Experimental

2.1. Materials

1-Methylimidazole (Aldrich, 99.0 %), 3-chloropropyltrimethoxysilane (Aldrich, 97.0 %), acetone (Vetec, 99.5 %), acetophenone (Merck, 98.0 %), carbon dioxide (Air Liquids, 99.998 %), dichlorometane (Vetec, 99.5 %), diethyl ether (AGA, 95.0 %), epichlorohydrin (Sigma-Aldrich, 99.0 %), glycidyl isopropyl ether (Sigma-Aldrich, 98.0 %), lithium(I) bis(trifluoromethanesulfonyl)imide (Sigma Aldrich, 99.0 %), propylene carbonate (Merck, 99.7 %), propylene oxide (Sigma-Aldrich, 99.0 %), sodium hydroxide (Vetec, 99.0 %), sodium hexafluorophosphate (Alfa Aesar, 99.0 %), sodium tetrafluoroborate (Acros Organics, 98.0 %), styrene oxide (Sigma Aldrich, 97.0 %), titanium dioxide (JB Química, TiO_2, 98.0 % anatase phase), toluene (Merck, 99.9 %), zinc bromide (Sigma Aldrich, 98.0 %) were used as received.

2.2. Preparation of catalysts

2.2.1. Titanate nanostructures synthesis

Titanate nanostructures (TNT) were synthesized by hydrothermal method as described in literature [25]. In a typical procedure, 1.5 g (18.7 mmol) of TiO_2 was added to 120 mL of NaOH solution 10 mol.L^{-1} under magnetic stirring at room temperature for 30 min. The solution was then transferred to a stainless steel reactor (200 cm^3) internally coated with Teflon® maintained for 72 h at 135 °C. Lastly a white precipitate was separated by centrifugation, washed with distilled water until pH = 8 and dried at 80 °C for 6 h.

2.2.2. Ionic liquid synthesis

The 1-methyl-3-(3-trimethoxysilylpropyl)imidazolium chloride ([$(MeO)_3Sipmim$][Cl]) was prepared by the reaction of 1-methylimidazole with 3-chloropropyl trimethoxysilane (molar ratio 1:1.5) under reflux in toluene (95 °C) and under nitrogen flow for 48 h, as described in literature [24,26]. The mixture was cooled to room temperature. The organic upper phase corresponding to the ionic liquid was then separated, washed with diethyl ether and dried at 50 °C for 8 h. The resulting product was a yellow viscous ionic liquid.

2.2.3. Ionic liquid supported on titanate nanostructures

The immobilization of the ionic liquid on the nanostructures was carried out following the literature [24]. In a typical procedure, 1 g (3.3 mmol) of TNT and 1 g (3.5 mmol) of [$(MeO)_3Sipmim$][Cl] IL were added to 20 mL of dry toluene. This mixture was kept under stirring at 90 °C for 16 h. After filtration, unreacted IL was then removed by extraction (Soxhlet method) for 8 h using dichloromethane. The solid obtained was dried under reduced pressure and named as TNT-[IL][Cl] hybrid nanostructure.

To obtain the other hybrid nanostructures named TNT-[IL][X] (where, IL = $(MeO)_3Sipmim$ and X = [BF_4^-], [PF_6^-] and [Tf_2N^-]), 1 g (3.4 mmol) of TNT-[IL][Cl] were added to an equimolar solution of $NaBF_4$, $NaPF_6$ (in acetone) or $LiTf_2N$ (in distilled water/acetone mixture 1:1 v/v) under magnetic stirring at room temperature for 24 h.

The TNT-[IL][X] solids were separated by simple filtration and the salt excess (NaCl or LiCl) was removed by washing with distilled water. All materials were dried under reduced pressure.

The molar weight (MW) of the catalysts was determined by ponderal calculation described in the Eq. (1), as described in literature [24]:

$$MW_{IL\text{-}TNTs} = (MW_{TNTs} \times \%TNT) + (MW_{IL} \times \%IL) \quad (1)$$

where:

MW_{TNTs} = molar weight of TNTs (301.7 g mol^{-1});
MW_{IL} = molar weight of IL;
%TNT = amount of TNT in the catalysts determined by TGA;
%IL = amount of IL in the catalysts determined by TGA.

2.3. Catalytic reactions

The reactions were performed in a 120 cm^3 stainless steel autoclave equipped with magnetic stirring. In a typical procedure, 1.5 mol% of catalyst (based on epoxy amount), 0.33 mmol of cocatalyst ($ZnBr_2$) and 50 mmol of epoxide were placed in the reactor, without the use of any solvent. Styrene oxide (SO) was chosen as a model substrate to evaluate the reactional parameters, such as temperature, time and CO_2 pressure. The reactions were carried out in a temperature range of 70–160 °C, a pressure range of 2–5 MPa and time reaction of 2 and 4 h, being these conditions determined based on the literature [27].

At the end of the reaction, the reactor was cooled to room temperature and slowly depressurized. The liquid reaction products were separated from the catalyst by simple filtration, weighted and analyzed by gas chromatography after being diluted in diethyl ether. A gas chromatograph Shimadzu CG-2014 equipped with a flame ionization detector (FID) and a 100 % dimethyl polysiloxane column, 30 m, 0.53 mm ID was used. Propylene carbonate was used as an internal standard to styrene oxide, epichlorohydrin and glycidyl isopropyl ether reactions and acetophenone to propylene oxide reaction. The turnover number (TON) and turnover frequency (TOF) was calculated according to Eqs. (2) and (3).

$$TON = \frac{\text{mmol of product}}{\text{mmol of catalyst}} \quad (2)$$

$$TOF = \frac{TON}{\text{time (h)}} \quad (3)$$

2.4. Characterization

2.4.1. Morphological analysis

To morphological evaluation of the TNT-[IL][X] hybrid

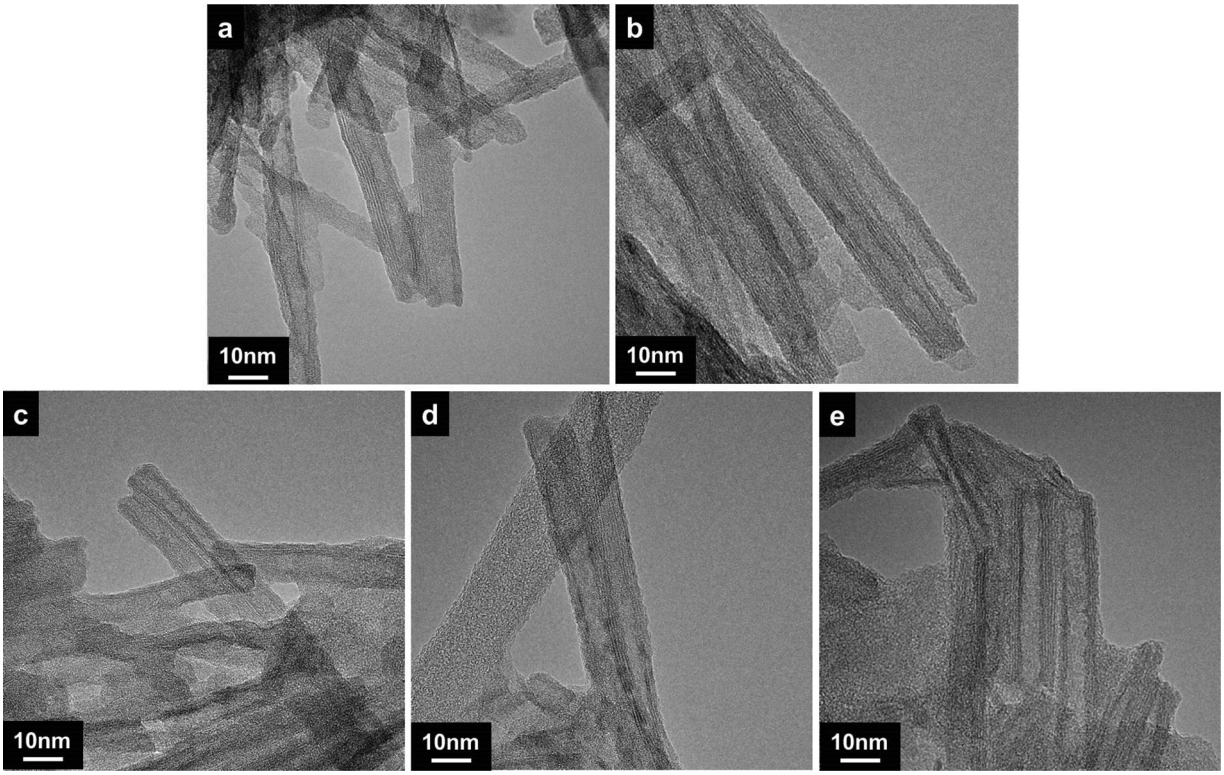

Fig. 1. TEM micrographs of (a) TNT, (b) TNT-[IL][Cl], (c) TNT-[IL][BF_4], (d) TNT-[IL][PF_6] and (e) TNT-[IL][Tf_2N], magnification of 440 k.

nanostructures was carried out through transmission electron microscopy analyses (TEM, FEI Tecnai G2 T20). Samples were deposited on carbon film coated copper grids of 300 mesh. All samples were analyzed as powder. The measure of external diameter were performed by *Image J* software.

2.4.2. Fourier transform infrared spectroscopy (FTIR)

FTIR analyses were performed from samples in powder at room temperature in UATR mode, in the range of 4000–650 cm^{-1}, on a PerkinElmer spectrometer (Spectrum One model). Following the assignments obtained by FTIR for TNT and TNT-[IL][X] hybrid nanostructures.

TNT: FTIR ν (cm^{-1}): 3400–3300 (surface OH groups), 1640 (H—O—H), 900 (Ti-O).

[$(MeO)_3$Sipmim][Cl]: ν (cm^{-1}): 3030 (Si—OH), 2944 (C—H of CH_2), 2839 (C—H of CH_3), 1570-1460 (C═C aromatic), 1248 (C—N aromatic), 1070–1175 (Si—O—CH_3), 805 (Cl).

TNT-[IL][Cl]:FTIR ν (cm^{-1}): 3400-3300 (surface OH groups), 3090 (Si—OH), 2938 (C—H of CH_2), 2891 (C—H of CH_3), 1630 (H—O—H), 1571-1450 (C═C aromatic and C—N aromatic), 1085–1185 (Si—O—CH_3), 900 (Ti—O), 736 (Cl).

TNT-[IL][BF_4]:FTIR ν (cm^{-1}): 3400-3300 (surface OH groups), 3096 (Si—OH), 2935 (C—H of CH_2), 2891 (C—H of CH_3), 1632 (H—O—H), 1572-1455 (C═C aromatic and C—N aromatic), 1052 (B—F), 1077–1198 (Si—O—CH_3), 900 (Ti—O), 744 (B—F).

TNT-[IL][PF_6]:FTIR ν (cm^{-1}): 3400-3300 (surface OH groups), 3122 (Si—OH), 2969 (C—H of CH_2), 2892 (C—H of CH_3), 1630 (H—O—H), 1574-1457 (C═C aromatic and C—N aromatic), 1054–1199 (Si—O—CH_3), 888 (Ti-O), 835 (P—F).

TNT-[IL][Tf_2N]:FTIR ν (cm^{-1}): 3400–3300 (surface OH groups), 3097 (Si—OH), 2940 (C—H of CH_2), 2868 (C—H of CH_3), 1631 (H—O—H), 1570–1457 (C═C aromatic and C—N aromatic), 1056–1193 (Si—O—CH_3), 884 (Ti—O), 785 (N—S), 735 (C—S), 675 (C—F).

2.4.3. X-ray diffraction analysis (XRD)

The crystalline structures of the hybrid nanostructures were investigated performing XRD analyses (Shimadzu XRD 7000) using the Kα radiation of the copper (λ = 1.542 Å), 40 kV, 30 mA, between 5°–70° 2θ, a scan of 0.02° and counting time of 2.0 s. The interlamellar distance was calculated using the Bragg equation [28].

2.4.4. Nitrogen adsorption-desorption isotherms

The nitrogen adsorption-desorption isotherms were recorded at 77 K in the 0.010 a 1.05 bar relative pressure range using a pore and surface analyzer (Micromeritics Instruments Corporation, TriStar II 302 V1.03). Samples were degassed at 120 °C for 24 h under vacuum before analysis. Surface areas were calculated using Brunauer-Emmett-Teller (BET) method. The samples were analyzed as powder.

2.4.5. Thermogravimetric analysis

The thermal stability of the nanostructures, as well as, the percentage of IL anchored on titanate nanostructures were evaluated by TGA analyzes (TA Instruments Q600) carried out with a heating rate of 20 °C/min, from room temperature to 1000 °C under nitrogen flow. The samples were analyzed as powder.

2.4.6. Solid state NMR

The anchorage of ILs in the TNTs surface were evaluated by NMR measurements (^{29}Si MAS NMR) performed at room temperature on an Agilent 500 MHz equipment (model DD2), cross-polarization magic angle spinning (CPMAS). The spectra were recorded with pulses of 2.8 ms scans and delay of 5 s.

2.4.7. Computational methods

Density Functional Theory (DFT) calculations were performed using Becke`s three-parameter exchange functional [29] in combination with the Lee, Yang and Parr correlation functional (B3LYP) [30] with a 6-311 + + G(d,p) basis set as implemented in the GAUSSIAN 16 package. Structures were fully optimized, under no symmetry constraints, and

vibrational frequency calculations were performed. Final structures have no imaginary frequencies associated with them. The frontier orbital energies and natural bond analysis (NBO) were calculated in single point runs in the same theory level. Molecular electrostatic potential maps (MEPs) of total electronic densities using the partial charges were analyzed with Gabedit software [31], with an isosurface value of 0.014181 and grid values from −0.08 to 0.08.

3. Results and discussion

3.1. Characterization of the catalysts

TEM images of the synthesized TNT and TNT-[IL][X] nanostructures are presented in Fig. 1. Fig. 1a shows that TNTs correspond to agglomerates of elongated rods with nanometric dimensions. These TNTs, which exhibit open or closed extremities have walls formed of multiple layers and an external diameter approximatively 8.8 ± 0.8 nm similar to found in the literature [32,33].

Figs. 1b-e show that the TNT morphology is not modified after the anchorage step of the IL. The external diameter values are 9.0 ± 0.6, 8.0 ± 1.6, 9.1 ± 0.6 and 9.6 ± 0.3 for TNT-[IL][Cl], TNT-[IL][BF_4], TNT-[IL][PF_6] and TNT-[IL][Tf_2N], respectively.

N_2 adsorption-desorption isotherms and pore size distribution are presented in Fig. 2. All samples showed a type IV isotherm, however, the hysteresis regions are distinct as well as the pores size distribution diagrams obtain for each material. Samples TNT-[IL][BF_4] and TNT-[IL][PF_6] present pores size in the mesopores range (2–20 nm) and hysteresis cycles (H3) at P/P_o between 0.5–1.0 and 0.7–1.0, respectively. The size of the hysteresis located at P/Po in the range 0.7–1.0 (Fig. 2a) and the pore size distribution (Fig. 2b) indicates that the pores volume and the diameter of the pores of TNT-[IL][PF_6] are higher than those of TNT-[IL][BF_4].

Isotherms hysteresis of TNT-[IL][Cl] and TNT-[IL][Tf_2N] located at P/Po = 0.9–1.0 are smaller than those of TNT-[IL][PF_6] and TNT-[IL][BF_4] (compare Fig. 2a with 2c) indicating that pore volume of the first cited nanostructures is smaller despite the pore diameter which is higher when compared with those of TNT-[IL][PF_6] and TNT-[IL][BF_4] (compare Fig. 2b with d).

The TNT's specific surface area (SSA) value is 155 m^2/g, but those of the hybrid materials TNT-[IL][Cl], TNT-[IL][BF_4], TNT-[IL][PF_6] and TNT-[IL][Tf_2N] are 1.5, 5.6, 42.0 and 1.7 $m^2 g^{-1}$ respectively showing the SSA decrease due to the TNT functionalization. This result indicates that the IL molecules cover the TNT surface avoiding the N_2 adsorption. According to the literature the anchoring of the IL molecules can occur through of the OH groups located at the surface of the TNTs [34].

The thermal behavior of the TNT and hybrid nanostructures is presented in Fig. 3. TNT suffer two weight losses corresponding to the water desorption (between 25–100 °C) and OH groups present in the TNT surface (between 100–200 °C), remaining stable after this temperature. The weight loss of all the TNT-[IL][Cl], TNT-[IL][BF_4] and TNT-[IL][PF_6] hybrid materials are similar and occur in three stages. The first stage is related to water and volatile compounds desorption (below 200 °C). The second and third steps (T_{peak} ≈ 300 and 500 °C) are related to the degradation of the alkyl radicals and imidazolium ring of the IL. In the case of TNT-[IL][Tf_2N], an intense degradation signal is observed at approximatively 460 °C indicating that the IL groups are degraded together in a single step (T_{peak} ≈ 460 °C).

In Table 1 are reported the weight loss corresponding to each temperature obtained TGA analysis. The amount of IL anchored on the TNT is determined from these data. As already mentioned, the weight loss recorded at 100–200 °C corresponds to water desorption from OH groups present at the TNT. The corresponding data reported in Table 1 indicate that the hybrid materials have less free OH groups than the pristine TNT. The weight loss for TNT-[IL][Cl], TNT-[IL][BF_4], TNT-[IL][PF_6] and TNT-[IL][Tf_2N] is respectively 9.4, 9.3, 9.7 and 4.7 %, while it is 13.0 % for TNT. The small weight loss recorded with TNT-[IL][Tf_2N] can be attributed to a smaller amount of OH groups remaining at the TNT surface.

The weight loss above 200 °C corresponds to IL decomposition and IL content of the hybrid materials. The values of 31.5, 20.9, 16.9 and 43.5 % for TNT-[IL][Cl], TNT-[IL][BF_4] and TNT-[IL][PF_6] and TNT-[IL][Tf_2N], respectively, are related to weight loss in the 200–700 °C range. The correlation between water loss and weight loss (in the range of 200–700 °C) can indicate that the IL is anchored through binding with the OH groups present at the surface of the TNT.

The anchorage of [$(MeO)_3$Sipmim][Cl] in the surface of TNTs was evaluated by ^{29}Si MAS-NMR (Fig. 4). Two significant peaks at -58 and -68 ppm, assigned to the three different environments of ^{29}Si atoms, were observed (Fig. 4). The T2 and T3 signals are assigned, respectively, to silicon atoms bonded to two and three condensed methoxy groups [35]. The correspondent values for each signal are 51 % for T2 and 49 % for T3.

TNT and hybrid nanostructure crystallinity were evaluated by XRD analysis (Fig. 5). TNT exhibited characteristic diffraction peaks located in 2θ = 10°, 24°, 28°, 48° and 62°, in agreement to literature [36–38]. In addition, TNT exhibited a monoclinic structure belonging to the P21/m space group. The diffuse peaks in 2θ between 30 - 45° and 62° are a result of the Na^+ intercalation [39]. Applying the Bragg equation to the

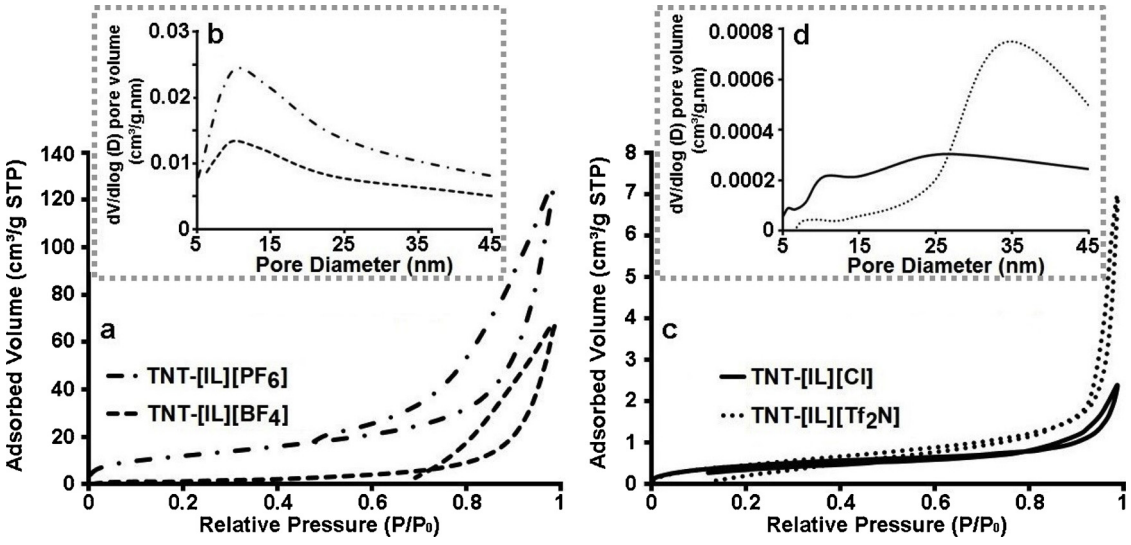

Fig. 2. N_2 adsorption–desorption isotherms (a,c) and distribution of pore diameter (b,d) of hybrid nanostructures.

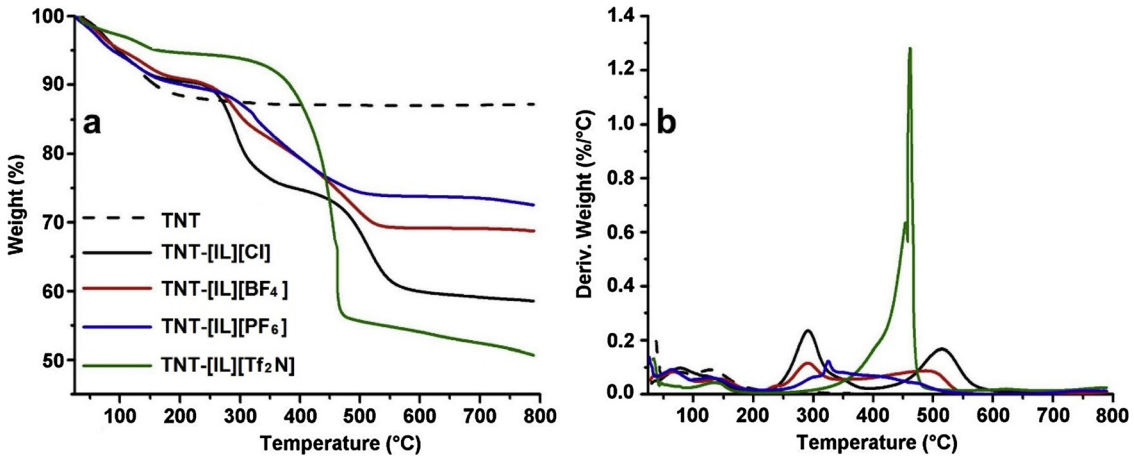

Fig. 3. TG (a) and DTG (b) curves of TNT and hybrid nanostructures.

Table 1
Amount of IL supported in the TNTs determined by TGA analysis.

Sample	Mass loss at 100 °C (%)	Mass loss at 100–200 °C (%)	Mass loss at 200–700 °C (%)	IL amount by TGA (%)
TNT	5.0	13.0 ± 0.7	0.8 ± 0.2	0.0
TNT-[IL][Cl]	5.1	9.4 ± 0.5	32.3 ± 0.9	31.5
TNT-[IL][BF_4]	5.0	9.3 ± 0.5	21.7 ± 0.5	20.9
TNT-[IL][PF_6]	5.2	9.7 ± 0.6	17.7 ± 0.5	16.9
TNT-[IL][Tf_2N]	2.0	4.7 ± 0.6	44.3 ± 0.6	43.5

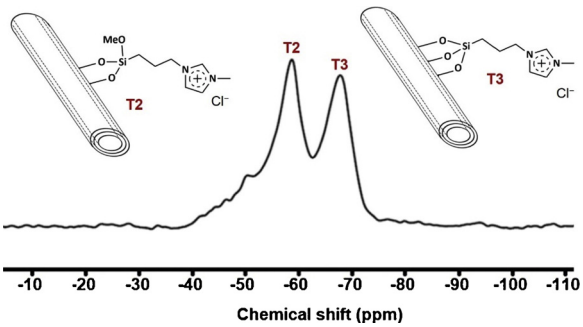

Fig. 4. ^{29}Si MAS-NMR spectrum of TNT-[IL][Cl].

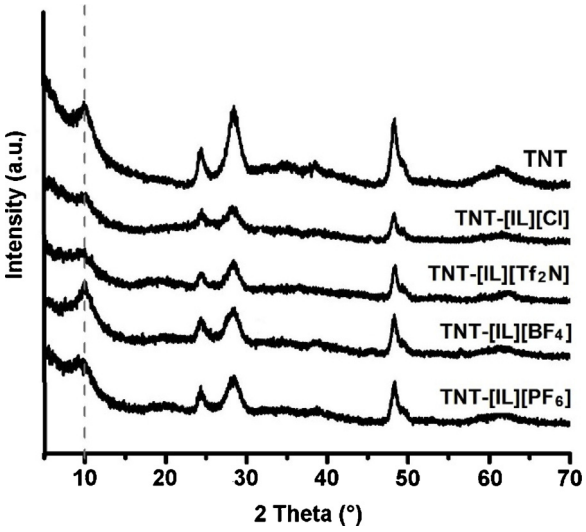

Fig. 5. XRD patterns of TNTs and hybrid nanostructures.

peak located in 2θ = 10° it is possible to obtain the interlayer distance. For TNT, TNT-[IL][Cl] and TNT-[IL][BF_4] the interlayer distance is 0.88 nm indicating that [$(MeO)_3$Sipmim][Cl] and [$(MeO)_3$Sipmim][BF_4] ILs do not modify the interlayer distance compared to pristine TNT. This indicates that these ILs were immobilized essentially on the TNT's surface. When TNT-[IL][PF_6] and TNT-[IL][Tf_2N] are used the interlayer distance values are 0.93 and 0.92 nm, respectively showing an increase when compared to the interlayer distance in the pristine TNT (0.88 nm). These results could indicate that [$(MeO)_3$Sipmim][PF_6] and [$(MeO)_3$Sipmim][Tf_2N] are located in the TNT interlayer. Niu et al. hypothesized this behavior could be due to the replaced of the Na^+ in the interlayer of TNTs, thus changed the original balance and enhanced the distance [40].

3.2. Catalytic activity

Based on recent studies of our group which describe the high activity of TNT-[IL][Cl] in cycloaddition reaction of CO_2 to propylene epoxide [24], this hybrid nanostructure was used as catalyst for the cyclic carbonates synthesis by the CO_2 coupling with styrene oxide (model substrate). In all reactions, $ZnBr_2$ was used as cocatalyst for its contribution in increasing the catalytic activity as a strong Lewis acid and assisting ring opening [7,24,41].

Blank tests were performed conducting experiments without the catalytic system (catalyst and cocatalyst) or in the presence of only the cocatalyst $ZnBr_2$. In all cases, no product was detected, in agreement with previous studies [24]. Additionally, reactions performed with pure IL (*i.e.* [$(MeO)_3$Sipmim][Cl]) presented very low activity (TOF of 1.0 h^{-1}). Fig. 6a shows that the best TOF values (higher than 10 h^{-1}) are achieved when the reactions are conducted at 100 °C or more, independently of the pressure value (range 2 − 5 MPa).

Fig. 6b shows that reaction times under 4 h yield low TON values are obtained (20.5 for 1 h and 35.5 for 2 and 3 h, respectively). TON increases with the increase of the reaction time, the equilibrium being attained in 4 h long (TON around 45). The strong rise in TON observed after the third hour might be attributed to the fact that the catalyst becomes more soluble in the medium containing increasingly carbonates, produced as the styrene oxide is converted, thus increasing reaction rate [42]. The decrease of TOF values reported in Fig. 6b indicates the occurrence of a deactivation process. This fact can be due to a leaching of the active species [43,44].

Considering the results obtained, the further reactions were performed at 100 °C, 4 MPa of CO_2 with two reaction times (2 h and 4 h). Reactions were conducted in these experimental conditions employing the hybrid catalyst described before to evaluate the influence of the IL's

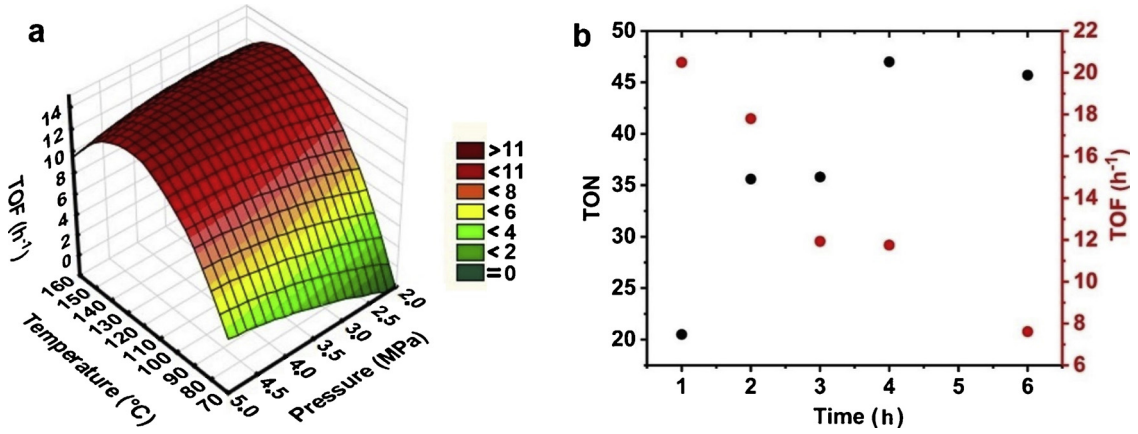

Fig. 6. Temperature - pressure effect (a) and time reaction (b) on the catalytic activity of TNT-[IL][Cl], (T = 100 °C and P_{CO2} = 4 MPa).

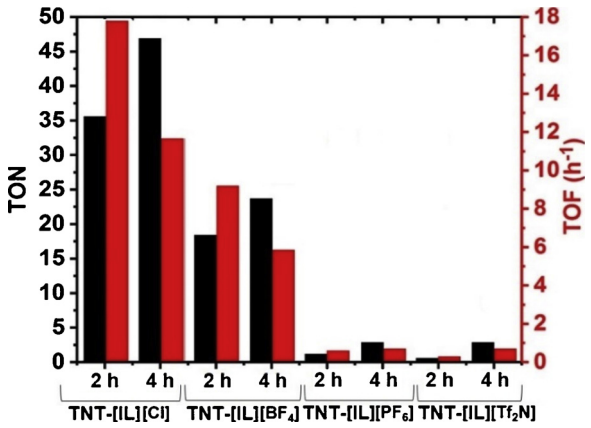

Fig. 7. Influence of the anion in the catalytic activity of the hybrid nanostructures in styrene carbonate synthesis by the CO_2 coupling with styrene oxide.

anion ([BF_4^-], [PF_6^-] and [Tf_2N^-]) in the carbonates synthesis by the CO_2 coupling with styrene oxide. The results of these studies presented in Fig. 7 show that the nanostructures TNT-[IL][PF_6] and TNT-[IL][Tf_2N] lead to low catalytic activity in 4 h of reaction (TON = 2.9 and TOF = 0.7 h^{-1}, for both catalysts) as well for 2 h of reaction (TON = 1.2 and 0.6, TOF = 0.6 and 0.3 h^{-1}, respectively).

The nanostructures that showed the best catalytic activity were TNT-[IL][Cl] and TNT-[IL][BF_4], in 2 h of reaction, obtaining a TON of 35.6 and TOF of 17.2 h^{-1} for TNT-[IL][Cl], while TNT-[IL][BF_4] showed a TON of 18.4 and TOF of 9.2 h^{-1}. In 4 h of reaction, these catalysts have improved even more their catalytic activity (TON = 47.0; TOF = 11.7 h^{-1} for TNT-[IL][Cl] and TON = 23.8; TOF = 5.9 h^{-1} for TNT-[IL][BF_4]). The difference in catalytic activity between these catalysts may be due to favorable nucleophilic attack of halide anion assisting in the opening of the epoxide ring [45].

Catalyst recyclability was evaluated for TNT-[IL][Cl] nanostructures, as showed in Fig. 8a. After each reaction, the catalyst was separated from the product by simple centrifugation and reused in the next reaction without any prior purification or wash. In the first recycling, the catalyst maintained the catalytic activity, as observed by TON and TOF values. Upon further recycling however, it observed a decrease in activity is observed, leading to values of TON = 7.9 and TOF = 1.9 h^{-1} in fourth recycling (loss of catalytic efficiency of ≈ 83 %). Oxygenated molecules like cyclic carbonates, epoxides and CO_2, can interact with the catalyst leading to its poisoning and deactivation [46].

In order to better investigate the loss of catalyst efficiency after the fourth recycling, it was separated by centrifugation and washed with acetone (three times), and dried at 60 °C for 2 h. This was done in order to purify the catalyst and reused in a new reaction. It was concluded that the catalyst was deactivated by poison/contaminants and after purification, the catalyst recovery 82 % of its efficiency (TON of 38 and TOF of 9.7 h^{-1}). The TEM analysis of spent catalyst after all recycles show that the tubular morphology was not affected (Fig. 8b–c).

Catalytic mechanism of the formation reaction of carbonates from CO_2 and epoxides is well described in the literature [24,47], where the key step of the CO_2/epoxide coupling mechanism is epoxide ring opening by the halide action [48]. This reaction occurs by a nucleophilic attack of the catalyst on the less hindered carbon atom of the epoxide ring. Stage 1 occurs with the coordination of the catalyst with the CO_2 molecule (Fig. 9). The cocatalyst $ZnBr_2$ acts as a Lewis acid and assists in opening the epoxide by the coordination with oxygen in epoxide (Stage 2). Concomitantly with these steps, the CO_2 coordinated with catalyst attack the less hindered carbon producing the alkylcarbonate anion (Stage 3) that will be converted into the cyclic carbonate by intermolecular cyclic elimination, regenerating the catalyst and cocatalyst [7,24].

Some studies have investigated the formation of cyclic carbonates with different epoxy substrates *via* CO_2 cycloaddition [14,47]. Among the main epoxies are the propylene oxide (PO), glycidyl isopropyl ether (GIE), epichlorohydrin (ECH) and styrene oxide (SO). Both steric and electronic effects significantly affect the yields, and the literature reports that the reactivity tends to decrease increasing their alkyl length [49]. However, few studies investigate in more detail the influence of different epoxides structures in cyclic carbonates formation [9,14,47]. In this work we proposed the evaluation of four epoxides using computational methods based on frontier molecular orbital and molecular electrostatic potentials.

The TNT-[IL][Cl] hybrid nanostructure was chosen as catalyst to cyclic carbonates formation from different epoxides (Table 2), because it showed the highest efficiency in the reaction with styrene oxide (Figs. 7 and 8). The catalytic activity, in 4 h of reaction, for the different epoxides follows the order: epichlorohydrin > styrene oxide > glycidyl isopropyl ether > propylene oxide (Table 2).

In order to investigate on the higher reactivity of these carbonates, in special ECH and SO, electronic effects on the epoxides were evaluated. Calculated MEPs are shown in different colors, increasing from red to blue (Fig. 10). The results indicate that, in all epoxides, there are regions with positive potential are near the H atoms, especially the H bonding to C2 carbon atom, while the regions with negative potential are found near the oxygen atoms of the ring. The SO ring showed a more neutral density, whereas in other carbonates a negative density is observed. The electron withdrawing effect of chlorine (in the ECH) and oxygen (in the GIE) causes a shift in density toward these atoms and make the H atom bond to the C2 carbon more acid than in other epoxides.

As is well known, a small HOMO-LUMO energy gap implies low

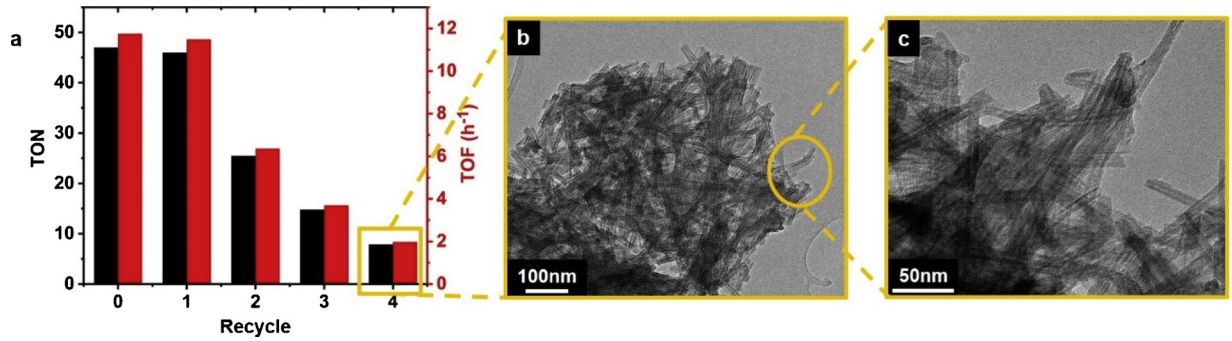

Fig. 8. Recycling experiments using TNT-[IL][Cl] as catalyst (a), TEM micrographs of spent catalyst (b,c), magnification of 64 and 180 k, respectively.

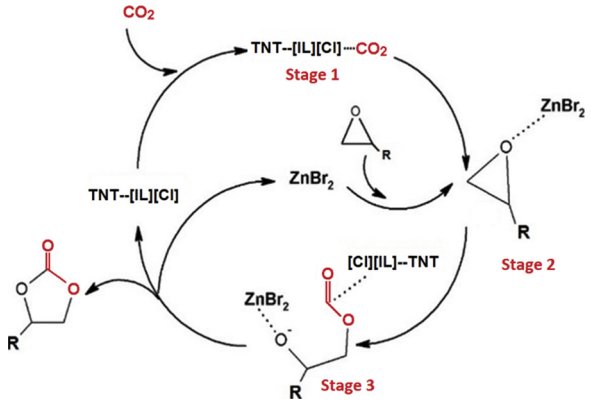

Fig. 9. Proposed mechanism for CO_2 cycloaddition to epoxides to form cyclic carbonates (R is the substituent on the epoxide ring).

Table 2
TON and TOF values of TNT-[IL][Cl] catalyst in the formation reaction of others cyclic carbonates using as epoxide propylene oxide (PO), glycidyl isopropyl ether (GIE), epichlorohydrin (ECH) and styrene oxide (SO).

Substrate	Product	TON	TOF (h^{-1})
(PO)		11.8	2.95
(GIE)		24.0	6.0
(ECH)		86.3	21.6
(SO)		47.0	11.75

Reaction conditions: 50 mmol of epoxide, 1.5 % mol of catalyst. 0.33 mmol of $ZnBr_2$, T = 100 °C, initial CO_2 pressure 4.0 MPa, t = 4 h.

kinetic stability because it is energetically favorable to add electrons to a low-lying LUMO and to receive electrons from a high-lying HOMO. This is a possible explanation of the SO reactivity found in this study. Other studies report that this epoxide shows itself with low reactivity when compared other epoxides due to the steric hindrance [15,42]. However, in this study, SO exhibited high reactivity which can be associated with a lower stability due to the smaller energy gap (ΔE = 6.143 eV) of HOMO-LUMO orbitals (Fig. 10). Similarly, GIE and PO present energy gaps slightly larger (ΔE = 6.870 eV and 7.370 eV, respectively) than SO, leading to relatively lower reactivities. In this line of thought, one would expect that ECH would be the least reactive of all tested epoxides, since ECH is the more stable structure, having the biggest HOMO-LUMO energy gap (ΔE = 7.491 eV). However, this did not occur. One possible explanation lies in the fact that LUMO orbital of ECH is delocalized over carbon atoms, in particular those belonging to epoxide ring. A highly delocalized LUMO indicates that the electrons can more readily move around the molecule [50].

The HOMO-LUMO energy gap possibilities the obtained important global reactivity descriptors, such as chemical hardness (η), global softness (S), chemical potential (μ), electronegativity (χ) and global electrophilicity (ω) that according to the Koopmans' theorem can be express as follows [51]:

$$\eta = \frac{1}{2}(\varepsilon\text{LUMO} - \varepsilon\text{HOMO}) \quad (4)$$

$$S = \frac{1}{2\eta} \quad (5)$$

$$\chi = -\frac{1}{2}(\varepsilon\text{HOMO} + \varepsilon\text{LUMO}) \quad (6)$$

$$\mu = \frac{1}{2}(\varepsilon\text{HOMO} + \varepsilon\text{LUMO}) \quad (7)$$

$$\omega = \frac{\mu^2}{2\eta} \quad (8)$$

The results of these global reactivity descriptors are presented in Table 3. Hardness is indicative of a molecule's ability to be polarized while softness is indicative of its ability to accept electron [52]. SO is the less harness structure, following by GIE, which can explain their activity reactive of the catalyst reacting with these epoxides. Another important parameter to be analyzed is the electronegativity of ECH, which is bigger than other ones epoxides. Electronegativity describe the ability of a molecule to attract electrons to itself [52].

To gain a deeper insight into the electronic nature of the intramolecular interaction contacts, we have performed an NBO analysis. The interaction or stabilization energy ($E^{(2)}$) is considered as a powerful tool to predict intra and inter-molecular charge transfer interactions in a molecule [53]. The larger the E(2) value, the more intensive is the interaction between electron donors and acceptors [54]. For atoms in the ring, higher interaction energies are observed for (σ) C1-O as donor and (σ^*) C2-O as acceptor, for all epoxides. The energies (in kcal. mol^{-1}) were 5.22 (PO), 5.11 (GIE), 5.01 (ECH) and 5.00 (SO). These results indicate that the ring of ECH and SO rings are less stable that those of PO and GIE.

These results show that SO has high reactivity due to the lower stability, as showed by HOMO-LUMO energy gap, hardness and NBO analyses. The ECH, despite the stability of its structure (see energy gap values, Fig. 10), has considerable electronegativity due to electron withdrawing by chlorine atom that generates the higher molecule electronegativity [46]. Besides that, a smaller donor -acceptor interaction energy is observed which may favor the opening of the ring. In GIE, the electron withdrawing effect by the oxygen is less significant. These results associated with hardness values justify the intermediary stability of GIE.

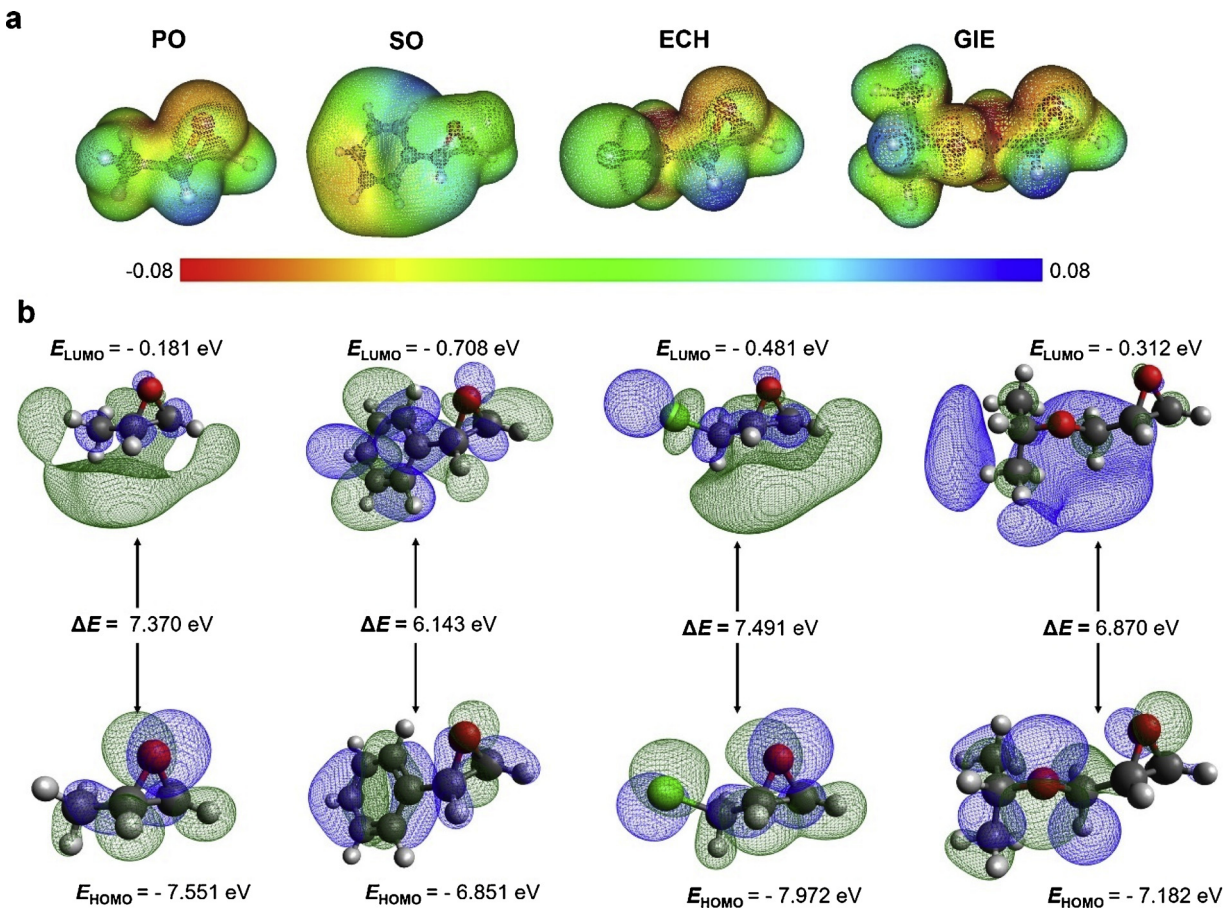

Fig. 10. (a) Molecular electrostatic potential and (b) molecular orbital surfaces of propylene oxide (PO), styrene oxide (SO), epichlorohydrin (ECH) and glycidyl isopropyl ether (GIE).

Table 3
Frontier molecular orbital parameters for propylene oxide (PO), styrene oxide (SO), epichlorohydrin (ECH) and glycidyl isopropyl ether (GIE).

Parameter (eV)	PO	SO	ECH	GIE
Chemical Potential (μ)	−3.866	−3.780	−4.227	−3.747
Electronegativity (χ)	3.866	3.780	4.227	3.747
Hardness (η)	3.685	3.072	3.7455	3.435
Softness (S)	0.1356	0.1627	0.1334	0.1455
Eletrofilicity (ω)	2.279	2.325	2.385	2.044

4. Conclusion

In this study, hybrid nanostructures based on TNT and IL were synthesized and characterized. The influence of the anion in the ionic liquid was evaluated and the best anchorage results were obtained with $[Cl^-]$ and $[Tf_2N^-]$. The functionalization with IL does not promote any change in the tubular morphology. These nanostructured materials were used as catalysts in the synthesis of styrene carbonate and the best results were obtained using TNT-[IL][Cl]. Moreover, proved to be a highly efficient catalyst for other epoxides (*i.e.* propylene oxide, epichlorohydrin, and glycidyl isopropyl ether). By using computational methods, it was possible propose explanations the reactivity of different epoxides. Styrene oxide, despite offering considerable steric hindrance, is the least stable structure. The electron withdrawing effect it is decisive to the reactivity of epichlorohydrin but is much less pronounced in the structure of glycidyl isopropyl ether.

Declaration of Competing Interest

None.

Acknowledgements

This study was financed in part by the Coordenação de Aperfeiçoamento de Pessoal de Nível Superior – Brasil (CAPES) – Finance Code 001. The authors would like to thank the National Research Council (CNPq), Pontifical Catholic University of Rio Grande do Sul (PUCRS) and the Federal University of Rio Grande do Sul (UFRGS) for technical support, the Central Laboratory of Microscopy and Microanalysis (LabCEMM/PUCRS) for the morphological analyses and the Theoretical Chemistry Group (TCG/UFRGS) for providing computational resources.

References

[1] Y.F. Liu, et al., Effects of operating parameters and ionic liquid properties on fabrication of supported ionic liquid membranes based on mesoporous γ-Al_2O_3 supports, J. Membr. Sci. 545 (September) (2018) 176–184 2017.
[2] E.I. Koytsoumpa, C. Bergins, E. Kakaras, The CO_2 economy: review of CO_2 capture and reuse technologies, J. Supercrit. Fluids 132 (2018) 3–16.
[3] G. Kupgan, et al., Modeling amorphous microporous polymers for CO_2 capture and separations, Chem. Rev. 118 (11) (2018) 5488–5538.
[4] B. Jia, J.S. Tsau, R. Barati, A review of the current progress of CO_2 injection EOR and carbon storage in shale oil reservoirs, Fuel 236 (July) (2019) 404–427 2018.
[5] A. Rafiee, et al., Trends in CO_2 conversion and utilization: a review from process systems perspective, J. Environ. Chem. Eng. 6 (5) (2018) 5771–5794.
[6] M.O. Vieira, et al., Chemical conversion of CO_2: evaluation of different ionic liquids as catalysts in dimethyl carbonate synthesis, Energy Procedia 114 (November) (2017) 7141–7149 2016.
[7] M.O. Vieira, et al., Surface active ionic liquids as catalyst for CO_2 conversion to

propylene carbonate, Catal. Lett. 148 (1) (2018).
[8] L. Ji, et al., Imidazolium ionic liquids/organic bases: efficient intermolecular synergistic catalysts for the cycloaddition of CO_2 and epoxides under atmospheric pressure, Mol. Catal. 446 (2018) 124–130.
[9] Y. Wu, et al., 3D-monoclinic M–BTC MOF (M = Mn, Co, Ni) as highly efficient catalysts for chemical fixation of CO_2 in to cyclic carbonates, J. Ind. Eng. Chem. 58 (2018) 296–303.
[10] B. Zou, C. Hu, Halogen-free processes for organic carbonate synthesis from CO_2, Curr. Opin. Green Sustain. Chem. 3 (2017) 11–16.
[11] L. Song, et al., UTSA-16 as an efficient microporous catalyst for CO_2 conversion to cyclic carbonates, Microporous Mesoporous Mater. 241 (2) (2017) 36–42.
[12] B. Chatelet, et al., Role of pre-organization around the azaphosphatrane catalyst's active site in the conversion of CO_2 to cyclic carbonates, Catal. Commun. 52 (2014) 26–30.
[13] J.-J. Chen, Z.-L. Gan, X.-Y. Yi, Dinuclear silver complexes for solvent-free catalytic synthesis of cyclic carbonates from epoxides and CO_2 at ambient temperature and pressure, Catal. Lett. 148 (3) (2018) 852–856.
[14] S. Baj, et al., Catalytic coupling of epoxides and CO_2 to cyclic carbonates by carbon nanotube-supported quaternary ammonium salts, Appl. Catal. A Gen. 488 (2014) 96–102.
[15] M. Sankar, et al., Supported imidazole as heterogeneous catalyst for the synthesis of cyclic carbonates from epoxides and CO_2, Catal. Commun. 59 (2015) 201–205.
[16] M. Liu, et al., Zwitterionic imidazole-urea derivative framework bridged mesoporous hybrid silica: a highly efficient heterogeneous nanocatalyst for carbon dioxide conversion, ChemCatChem 9 (2017) 1–10.
[17] F. Héroguel, et al., Controlled deposition of titanium oxide overcoats by non-hydrolytic sol gel for improved catalyst selectivity and stability, J. Catal. 358 (2018) 50–61.
[18] S.J. Hoseini, et al., Multi-metal nanomaterials obtained from oil/water interface as effective catalysts in reduction of 4-nitrophenol, J. Colloid Interface Sci. 513 (2018) 602–616.
[19] Y. Zeng, et al., Nanostructured ultrathin catalyst layer based on open-walled PtCo bimetallic nanotube arrays for proton exchange membrane fuel cells, Nano Energy 34 (February) (2017) 344–355.
[20] Ö. Sönmez, et al., Influence of the addition of various ionic liquids on coal extraction with NMP, Fuel 212 (October) (2018) 12–18 2017.
[21] M.O. Vieira, et al., Ionic liquids composed of linear amphiphilic anions: synthesis, physicochemical characterization, hydrophilicity and interaction with carbon dioxide, J. Mol. Liq. 241 (2017) 64–73.
[22] T. Wang, et al., Acid-base bifunctional catalyst: Carboxyl ionic liquid immobilized on MIL-101-NH2for rapid synthesis of propylene carbonate from CO_2 and propylene oxide under facile solvent-free conditions, Microporous Mesoporous Mater. 267 (February) (2018) 84–92.
[23] J.N. Appaturi, F. Adam, ImX-MCM-41 (X = Cl, Br and I): active catalysts for the solvent free synthesis of phenyl glycidyl carbonate, Surf. Interfaces 14 (January) (2019) 305–313.
[24] W.F. Monteiro, et al., CO_2 conversion to propylene carbonate catalyzed by ionic liquid containing organosilane groups supported on titanate nanotubes/nanowires, Appl. Catal. A Gen. 544 (2017) 46–54.
[25] W.F. Monteiro, et al., Preparation of modified titanate nanotubes and its application in polyurethane nanocomposites, Macromol. Symp. 368 (1) (2016) 93–97.
[26] A.S. Aquino, et al., Rationalizing the role of the anion in CO_2 capture and conversion using imidazolium-based ionic liquid modified mesoporous silica, RSC Adv. 5 (79) (2015) 64220–64227.
[27] A. Jawad, F. Rezaei, A.A. Rownaghi, Porous polymeric hollow fibers as bifunctional catalysts for CO_2 conversion to cyclic carbonates, J. Co2 Util. 21 (August) (2017) 589–596.
[28] F.A. Rafiqi, M.S. Rather, K. Majid, Doping polyaniline with copper bisglycinate[Cu $(gly)_2$] - synthesis, characterization and thermal study, Synth. Met. 171 (2013) 32–38.
[29] A.D. Becke, Density-functional thermochemistry. III. The role of exact exchange, J. Chem. Phys. 98 (7) (1993) 5648–5652.
[30] C. Lee, W. Yang, R.G. Parr, Development of the Colle-Salvetti correlation-energy formula into a functional of the electron density, Phys. Rev. B 37 (2) (1988) 785–789.
[31] A.-R. Allouche, Gabedit—a graphical user interface for computational chemistry softwares, J. Comput. Chem. 32 (1) (2010) 174–182.
[32] R. Camposeco, et al., Behavior of Lewis and Brönsted surface acidity featured by Ag, Au, Ce, La, Fe, Mn, Pd, Pt, V and W decorated on protonated titanate nanotubes, Microporous Mesoporous Mater. 236 (2016) 235–243.
[33] L. Guo, et al., CO_2 removal from flue gas with amine-impregnated titanate nanotubes, Nano Energy 25 (2016) 1–8.
[34] W.F. Monteiro, et al., Modified titanate nanotubes for the production of novel aliphatic polyurethane nanocomposites, Polym. Compos. (2018) 1–9.
[35] L.F. Bobadilla, T. Blasco, J.A. Odriozola, Gold(Iii) stabilized over ionic liquids grafted on MCM-41 for highly efficient three-component coupling reactions, J. Chem. Soc. Faraday Trans. 15 (39) (2013) 16927–16934.
[36] J. Liu, et al., Polyethyleneimine functionalized protonated titanate nanotubes as superior carbon dioxide adsorbents, J. Colloid Interface Sci. 386 (1) (2012) 392–397.
[37] W. Liu, et al., Comparison on aggregation and sedimentation of titanium dioxide, titanate nanotubes and titanate nanotubes-TiO_2: influence of pH, ionic strength and natural organic matter, Colloids Surf. A Physicochem. Eng. Asp. 434 (2013) 319–328.
[38] W.F. Monteiro, et al., Dry reforming of methane using modified sodium and protonated titanate nanotube catalysts, Fuel 253 (2019) 713–721.
[39] D.C. De Carvalho, et al., Titanate nanotubes as acid catalysts for acetalization of glycerol with acetone: influence of the synthesis time and the role of structure on the catalytic performance, Chem. Eng. J. 313 (2017) 1454–1467.
[40] G. Niu, et al., Absorption of Cr(VI) onto amino-modified titanate nanotubes using 2-Bromoethylamine hydrobromide through SN2 reaction, J. Colloid Interface Sci. 401 (2013) 133–140.
[41] S. Zhong, et al., $ZnBr_2$/DMF as simple and highly active Lewis acid-base catalysts for the cycloaddition of CO_2 to propylene oxide, J. Co2 Util. 6 (2014) 75–79.
[42] J. Peng, et al., Chemical fixation of CO_2 to cyclic carbonate catalyzed by new environmental- friendly bifunctional bis-β-cyclodextrin derivatives, Catal. Today (January) (2018).
[43] X. Song, et al., Melem based multifunctional catalyst for chemical fixation of carbon dioxide into cyclic carbonate, J. Co2 Util. 24 (March) (2018) 287–297.
[44] Y. Wu, et al., Mn-based MOFs as efficient catalysts for catalytic conversion of carbon dioxide into cyclic carbonates and DFT studies, Chem. Eng. Sci. 201 (2019) 288–297.
[45] W. Cheng, et al., SBA-15 supported triazolium-based ionic liquids as highly efficient and recyclable catalysts for fixation of CO_2 with epoxides, Catal. Today 200 (1) (2013) 117–124.
[46] A. Samikannu, et al., Renewable N-doped active carbons as efficient catalysts for direct synthesis of cyclic carbonates from epoxides and CO_2, Appl. Catal. B 241 (August) (2019) 41–51 2018.
[47] M.O. Vieira, et al., Chemical fixation of CO_2: the influence of linear amphiphilic anions on surface active ionic liquids (SAILs) as catalysts for synthesis of cyclic carbonates under solvent-free conditions, React. Kinet. Mech. Catal. (2019).
[48] I. Karamé, et al., New zinc/tetradentate N4 ligand complexes: efficient catalysts for solvent-free preparation of cyclic carbonates by CO_2/epoxide coupling, Mol. Catal. 456 (June) (2018) 87–95.
[49] H. Chang, et al., Conversion of carbon dioxide into cyclic carbonates using wool powder-KI as catalyst, J. Co2 Util. 24 (August) (2018) 174–179 2017.
[50] G. Mahalakshmi, V. Balachandran, Nbo, Homo, Lumo analysis and vibrational spectra (FTIR and FT Raman) of 1-Amino 4-methylpiperazine using ab initio HF and DFT methods, Spectrochim. Acta 135 (2015) 321–334.
[51] A.O. Zacharias, et al., Dft, spectroscopic studies, NBO, NLO and Fukui functional analysis of 1-(1-(2,4-difluorophenyl)-2-(1H-1,2,4-triazol-1-yl)ethylidene) thiosemicarbazide, J. Mol. Struct. 1158 (2018) 1–13.
[52] H.F. Hizaddin, R. Anantharaj, M.A. Hashim, A quantum chemical study on the molecular interaction between pyrrole and ionic liquids, J. Mol. Liq. 194 (2014) 20–29.
[53] K.M. Al-Ahmary, M.M. Habeeb, S.H. Aljahdali, Synthesis, spectroscopic studies and DFT/TD-DFT/PCM calculations of molecular structure, spectroscopic characterization and NBO of charge transfer complex between 5-amino-1,3-dimethylpyrazole (5-ADMP) with chloranilic acid (CLA) in different solvents, J. Mol. Liq. 277 (2018) 453–470.
[54] V. Deepha, R. Praveena, K. Sadasivam, Dft studies on antioxidant mechanisms, electronic properties, spectroscopic (FT-IR and UV) and NBO analysis of C-glycosyl flavone, an isoorientin, J. Mol. Struct. 1082 (2015) 131–142.